Indirectly cooled secondary-particle production target at J-PARC Hadron Experimental Facility

Masayoshi Saito,[1,*] Keizo Agari,[2] Hironobu Akiyama,[2] Kazuya Aoki,[2] Erina Hirose,[2] Masaharu Ieiri,[2] Yohji Katoh,[2] Yusuke Komatsu,[2,§] Ruri Kurasaki,[2] Michifumi Minakawa,[2] Yuhei Morino,[2] Fumimasa Muto,[2] Yoshinori Sato,[2] Shinya Sawada,[2] Hitoshi Takahashi,[2,†] Toshiyuki Takahashi,[2] Kazuhiro Tanaka,[2] Akihisa Toyoda,[2] Hiroaki Watanabe,[2,‡] and Yutaka Yamanoi[2]

[1]*Tohoku University, 6-3 Aramaki Aza-Aoba, Aoba-ku, Sendai 980-8578, Japan*
[2]*High Energy Accelerator Research Organization (KEK), 1-1 Oho, Tsukuba, Ibaraki 305-0801, Japan*

(Received 20 December 2021; accepted 25 April 2022; published 3 June 2022)

The Hadron Experimental Facility at the Japan Proton Accelerator Research Complex is used for various nuclear and elementary particle physics experiments that use secondary particle beams. The secondary-particle production target is a key element for the generation of particles such as kaons and pions. To increase beam power, a new target was developed and installed. The target, which is made of gold and indirectly cooled with water, was designed so that the maximum stresses do not exceed the allowable stresses determined based on the pressure vessel standard. 95 kW is considered to be the maximum power of the primary proton beam for a 5.2-s beam duration. The new target was stably operated up to a power of 65 kW. In addition, beam position estimation based on multipoint temperature measurements of the target was demonstrated.

DOI: 10.1103/PhysRevAccelBeams.25.063001

I. INTRODUCTION

A. J-PARC

The Japan Proton Accelerator Research Complex (J-PARC) [1,2] is a high-intensity proton accelerator facility located in Tokai, Ibaraki, Japan. J-PARC has a linear accelerator (LINAC) [3] and two synchrotrons. Negative hydrogen ions from the ion source are accelerated to 400 MeV by a LINAC and then extracted to a 3-GeV accelerator [rapid-cycling synchrotron (RCS)] [4]. Then, the negative hydrogen ions are converted to proton beams and accelerated to 3 GeV by the RCS. The majority of the 3-GeV proton beams are extracted to the Materials and Life Science Experimental Facility (MLF) [5], and some are sent to the 30-GeV main ring (MR) [6]. The MLF utilizes neutron or muon beams generated by the intense 3-GeV proton beams. At the MR, proton beams accelerated up to 30 GeV are supplied to the Neutrino Experimental Facility [7] or the Hadron Experimental Facility [8,9].

B. Hadron Experimental Facility

The Hadron Experimental Facility (Fig. 1) was built mainly for particle and nuclear physics experiments. Various experiments are carried out using kaons or pions as the secondary-particle beams [10,11]. There are three secondary beam lines [12–15]. The K1.8 beam line can deliver charged kaons and pions up to 2.0 GeV/c. The K1.8BR beam line can deliver charged kaons and pions up to 1.1 GeV/c. The KL beam line [11,15] is a dedicated

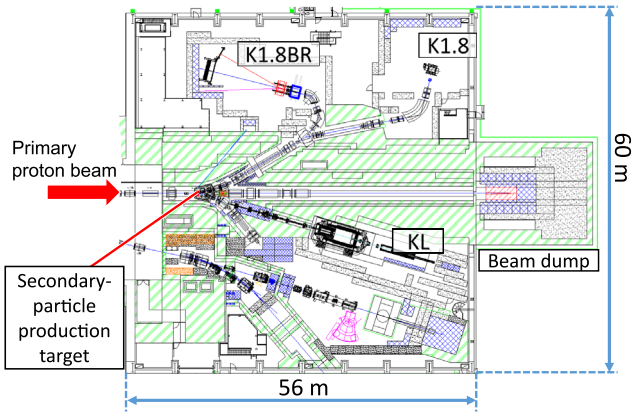

FIG. 1. Plan view of Hadron Experimental Facility.

*saito@lambda.phys.tohoku.ac.jp
†hitoshi.takahashi@kek.jp
‡hiroaki.watanabe@kek.jp
§Present address: TDSE Inc., Tokyo Operacity Tower 27F 3-20-2 Nishishinjuku, Shinjuku-ku, Tokyo 163-1427, Japan.

neutral kaon beam line for the study of the rare decay $K_L \to \pi^0 \nu\bar{\nu}$. The secondary particles used at these beam lines are generated at the production target located near the most upstream section of the Hadron Experimental Facility. Secondary particles, such as kaons and pions, are produced at the target by the primary proton beam. The secondary beams are delivered to the experimental areas by the secondary beam lines mentioned above. The primary beams that go through the production target are transported by the primary beam line and are finally absorbed by the beam dump.

C. Production target and beam conditions

The production target in the Hadron Experimental Facility has been replaced several times with new ones to accept higher beam power. The previous target [16] was used from 2014 until 2019 and could accept proton beams up to 50 kW. In total, 1.5×10^{20} protons irradiated the previous target, and no damage was observed.

To accept more intense proton beams, this target was replaced by a new target, as described in this paper. The power of the primary proton beams has been increased; 65-kW beams were achieved in 2021.

The standard deviation of the beam size at the production target is 2.5 mm (σ_H) in the horizontal direction and 1.0 mm (σ_V) in the vertical direction. Currently, the MR accelerator is operated with a repetition cycle of 5.2 s and the proton beams are extracted slowly for 2 s out of the 5.2 s in one cycle.

II. NEW TARGET

A. Target structure and materials

For the secondary beam lines, the most important goal is to provide intense, high-quality secondary beams (mainly kaons and pions). One of the most important qualities of the secondary beams is the separation of particle species (protons, kaons, pions, electrons, etc.). To obtain well-separated secondary beams, the production volume of the secondary particles at the target should be as small as possible. For charged particles, the vertical beam size (σ_V) is more important than the horizontal beam size (σ_H) because such particles are separated in the difference in their vertical orbits [12]. For neutral particles, both dimensions are important due to the configuration of the collimators [15]. The dimensions of the primary beam at the position of the target were thus decided to be 2.5 and 1.0 mm in the horizontal and vertical directions, respectively.

For the target material, properties such as density, strength, melting point, thermal conductivity, and coefficient of linear thermal expansion should be considered. Higher density is desirable because it increases the production rate of the secondary particles per unit volume. Higher thermal conductivity is desirable because it lowers the thermal resistance between the heat source and the cooling water. Stress and strain are generated at the bonded interface of two materials due to the difference in the coefficient of linear thermal expansion between the materials.

Gold was selected as the target material. Other materials, such as platinum, have a higher production rate of secondary particles but their thermal properties are worse. Tungsten was evaluated during the design of the previous target, but it was concluded that the design margin for the tungsten target was smaller than that for the gold target [16]. Figure 2 shows schematic drawings of the target. The upper and lower halves of the target were made separately and then assembled to make the complete target [Fig. 2(a)]. Figure 2(b) shows the lower half (the upper half has the same structure). The gold (K24) target was placed on a

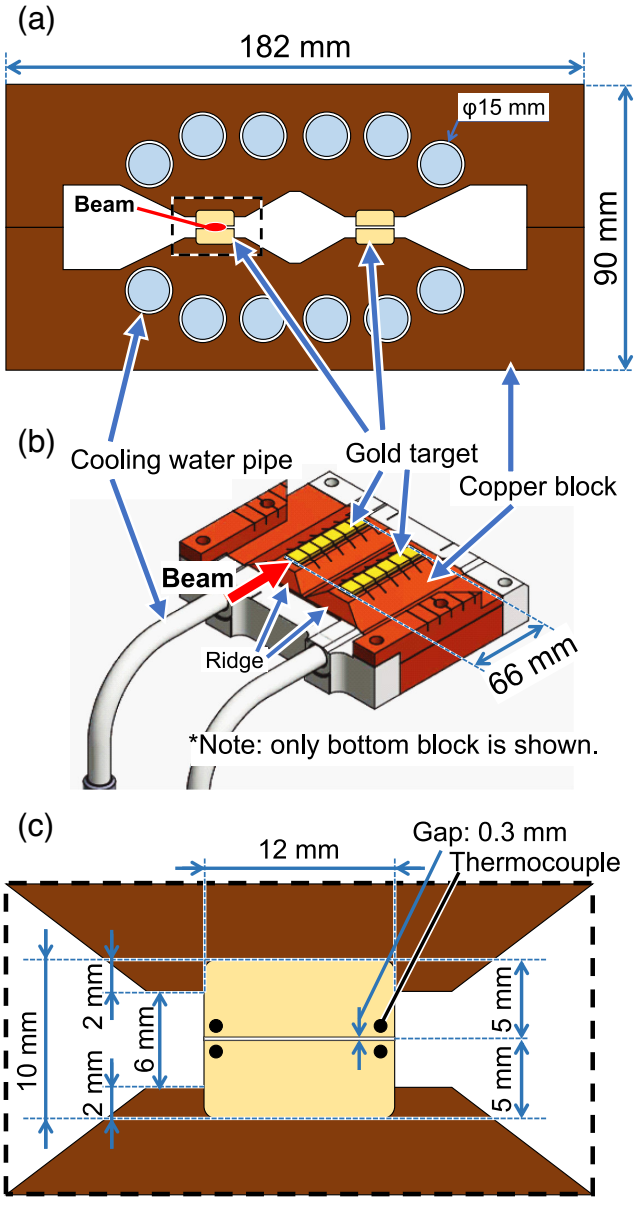

FIG. 2. Schematic drawings of new target: (a) cross-sectional view of target, (b) lower half of target, and (c) expanded view.

copper (C1020) pedestal in which water pipes made of stainless steel (SUS316L) were embedded. Hot isostatic pressing was used to bond the gold and copper. In this method, diffusion bonding is conducted by pressing the materials isostatically in a high-temperature atmosphere, which generally reduces defects in the bonded layer [17,18] and leads to good thermal conduction [19,20]. This method was applied to the previous target [16], for which no damage was found after beam operation, and is thus considered to be reliable for the new target.

The longitudinal size of the target affects the horizontal source size of secondary beams because the secondary beams are extracted at horizontal angles (6° for charged particles, 16° for neutral particles) with respect to the direction of the primary beam. Hence, the total length of the gold target was determined to be 66 mm. The gold was divided into six segments in the direction of the beam to reduce thermal stress. As shown in Fig. 2(c), the width of the target is 12 mm and the total height, including a 0.3-mm gap between the upper and lower gold blocks, is 10 mm. The gap was introduced to allow the thermal expansion of the target, as described in the following section. The gold is sunk in the copper block by 2 mm to improve the bonding strength. Primary protons are injected into the center of the upper and lower gold blocks, as shown in Fig. 2(a). The generated heat is shared between these blocks. Each copper block has two ridges. The gold blocks are bonded to each ridge. One of the two ridges is a spare. The ridges can be remotely swapped with each other by moving the copper blocks in the horizontal direction. This mechanism allows fast target exchange and the resumption of beam operation if one target is damaged. Figure 3 shows a photograph of the new target after assembly.

B. Thermal stress analysis

First, the criteria for allowable stress were determined for the thermal stress analysis. The criteria are mainly based on the pressure vessel standard [21]. The maximum thermal stress and fatigue strength are calculated using the following relations:

$$\text{(i) } S_M \times 3 \text{ for thermal stress;} \tag{1}$$

$$\text{(ii) } 10^4\text{-cycle fatigue strength} \times 1/2 \text{ for low-cycle fatigue; and} \tag{2}$$

$$\text{(iii) } 10^7\text{-cycle fatigue strength} \times 1/2 \text{ for high-cycle fatigue,} \tag{3}$$

where S_M is the design stress, which is adopted as the smaller value between [ultimate strength $(\sigma_{\text{ultimate}}) \times 0.85/3$] and [0.2% proof strength $(\sigma_{\text{proof}}) \times 0.85/1.5$] of bulk gold. The design margins, a factor of $0.85/3$ and a factor of $0.85/1.5$, were determined based on the standard for welding pipes [21]. Low-cycle fatigue refers to the fatigue caused by the temperature difference between the target temperature before the start of beam operation and that after thermal equilibrium is reached during beam operation. High-cycle fatigue refers to the fatigue caused by the temperature rise and fall due to each extraction of the beam during the 2-s beam-on duration. The typical temperature cycles that cause low- and high-cycle fatigue are shown in Fig. 4. The new target was planned to be used for up to 5 years and to be operated 125 days per year on average. The design life of the target is thus 15000 hours (125 days × 5 years). Considering this design life, the numbers of low and high cycles in a typical case correspond to 10^4 and 10^7 cycles, respectively. Given that the 10^4- and 10^7-cycle fatigue strengths of bulk gold are 0.7 and 0.4 times the ultimate strength of bulk gold, respectively [22,23], the low- and high-cycle fatigue strengths were determined to be $\sigma_{\text{ultimate}}/2$ and $\sigma_{\text{ultimate}}/3$, respectively. The design margin for fatigue, which is a factor of 1/2 in Eqs. (2) and (3), was also determined based on the pressure vessel standard [21].

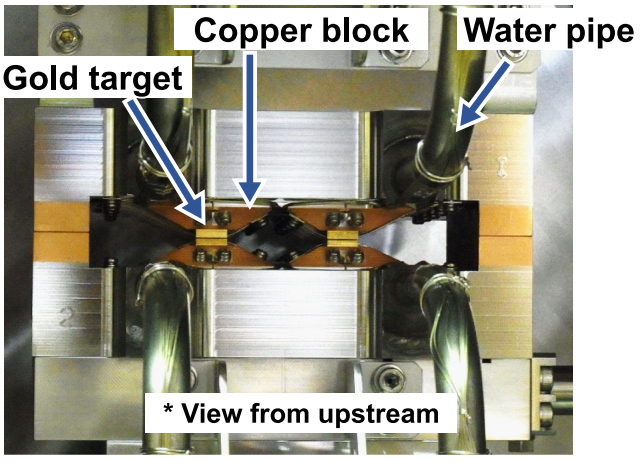

FIG. 3. Photograph of front view of new target after assembly.

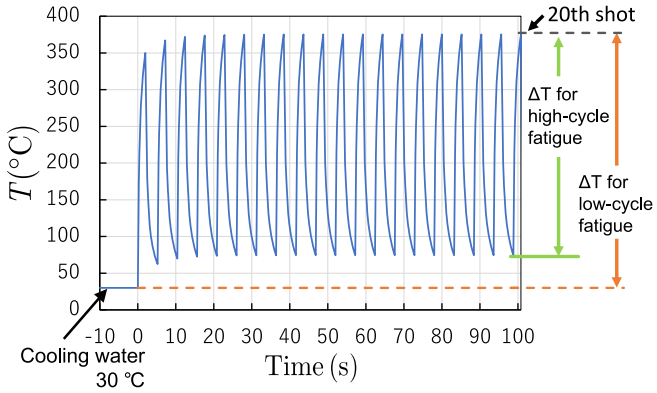

FIG. 4. Typical temperature cycles for gold calculated with beam power of 95 kW. The beam operation started at 0 s in the calculation. The definitions of the temperature difference (ΔT) for each type of fatigue are shown on the right side.

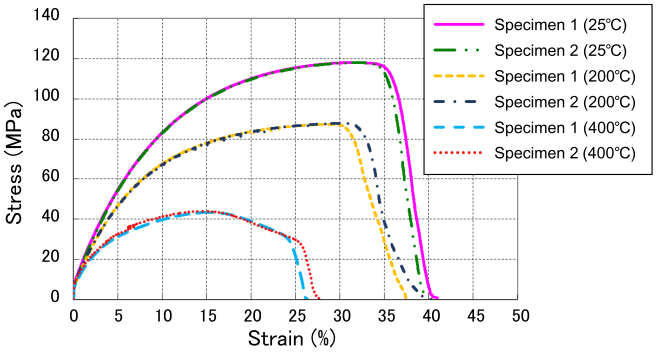

FIG. 5. Stress-strain curves obtained from tensile tests with gold specimens at several temperatures. The horizontal axis shows the engineering strain in the specimen (%) and the vertical axis shows the engineering stress (MPa). The tests were performed with the specimens at 25, 200, and 400℃.

The stress-strain curves for gold at several temperatures were obtained using tensile tests with rolled gold specimens (13B in the tensile testing standard) [24]. The same heat treatments as those in the actual fabrication process for the target were applied to the specimens before the tensile tests. Figure 5 shows the stress-strain curves obtained from tensile tests performed on two specimens at each temperature. For the evaluation, we used the average of the results for each specimen pair. Table I shows the values of the ultimate and 0.2% proof strengths obtained from the tensile tests. Shear tests were carried out on the bonded interfaces between the gold and copper at the same temperatures as those in the tensile tests (25, 200, and 400℃) because the difference in thermal expansion causes mainly shear stress at the bonded interfaces. The results confirmed that the fracture strength of the bonding was higher than the bulk gold strength.

The heat generation distribution in the target caused by the primary beam was simulated with the Monte Carlo code MARS-15 [25,26]. Then, the time dependence of the temperatures and stresses was calculated using thermal stress analysis software with the finite element method (ANSYS v12.0.1) [27]. In the simulation, the power of the primary beam was set to 95 kW and the repetition cycle of the accelerator was set to 5.2 s with 2-s beam irradiation of the target. The beam position was the center of the target. The primary beam was assumed to have a Gaussian shape with $\sigma_H = 2.5$ mm and $\sigma_V = 1.0$ mm. Although the beam loss at the target was about 50%, the heat deposition at the target was 7.4 kW. The target was cooled by water (heat transfer coefficient: 10000 $W/m^2/K$). Because the temperature rise of the cooling water was expected to be only 2℃, the temperature of the water was set to a constant value of 30℃. Surface cooling by He gas (heat transfer coefficient: 10 $W/m^2/K$) was also applied. The temperature of the gas was set to 30℃. Figure 6(a) shows the temperature distribution after the temperature rise became stable. Figure 6(b) shows the distribution of the von Mises equivalent stress. In the simulation, the maximum temperature of the gold was 375℃ and that of the bonded interfaces between the gold and copper was 264℃. These maximum temperatures are sufficiently lower than the melting points of gold and copper. The thermal stress was calculated based on the stress-strain curves (Fig. 5)

TABLE I. Results of tensile tests for bulk gold.

Temperature (℃)	Ultimate strength (MPa)	0.2% proof strength (MPa)
25	118	8.6
200	87	7.8
400	43	7.6

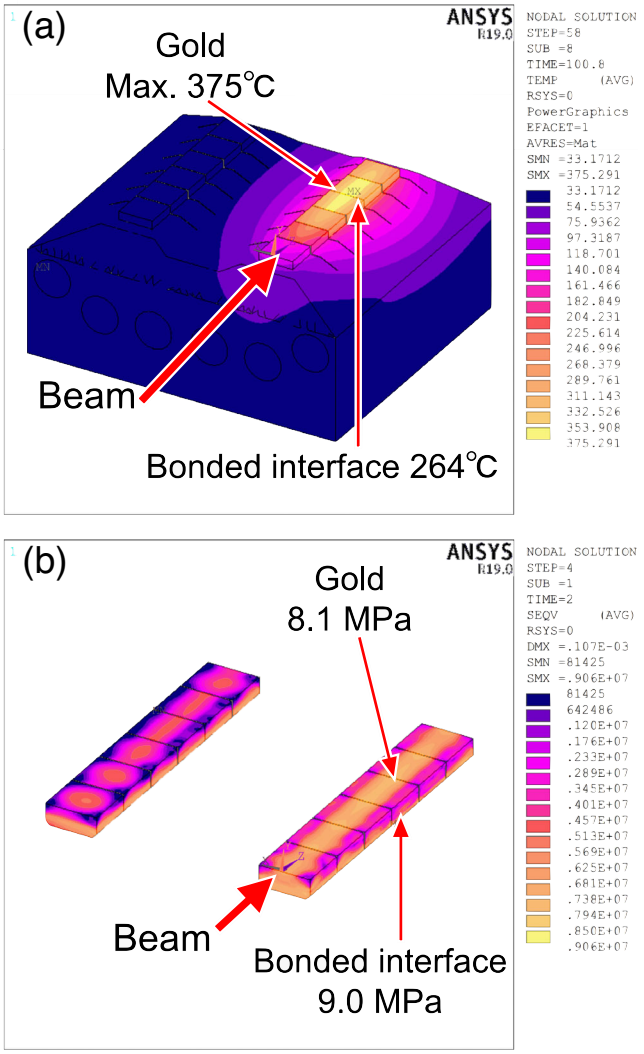

FIG. 6. Simulation results for (a) temperature distribution and (b) von Mises equivalent stress for new target irradiated with beam. ANSYS thermal stress analysis software was used. In this simulation, a beam power of 95 kW and a repetition cycle period of 5.2 s were assumed. The large red arrow indicates the direction of the beam. Only the lower half of the new target is shown.

TABLE II. Stress evaluation results for new target irradiated with 95-kW beam for 5.2 s.

Location (maximum temperature)	Stress classification	Calculated stress (MPa)	Allowable stress (MPa)
Gold (375°C)	Thermal	8.1	13.0
	High-cycle fatigue	7.9	8.1
	Low-cycle fatigue	8.2	12.2
Bonded interface (264°C)	Thermal	9.0	13.2
	High-cycle fatigue	9.0	12.2
	Low-cycle fatigue	9.2	18.3

using an elastic-plastic analysis that took plastic deformation into account. Based on the results, the maximum value of the von Mises equivalent stress was 8.1 MPa in the gold and 9.0 MPa at the bonded interfaces between the gold and copper. Since the calculated stresses were larger than σ_{proof} (Table I), plastic deformation is caused. Because only heat load is applied for the target by the beam irradiation, only thermal stress ("secondary stress") is generated while no mechanical stress ("primary stress") is generated, where the primary and secondary stresses are defined in the pressure vessel standard [21]. Based on the Bree diagram [28], the stress-strain behavior by the cyclic secondary stress without the primary stress is converged to plastic cycling, i.e., repeating a same hysteresis loop, and thus progressive plastic deformation is converged and does not directly lead to failure. For this case, the main cause of failure is considered to be fatigue due to the cyclic stress. The stress for fatigue was calculated from the alternating stress amplitude between the lowest and highest temperatures shown in Fig. 4. Table II shows the simulation results for the stress ("Calculated stress") and the allowable stress described above. The calculated stresses are lower than the corresponding allowable stresses. The calculated stress for the high-cycle fatigue for the gold is close to the allowable stress, and thus the maximum beam power was determined to be 95 kW.

The maximum vertical displacement due to thermal expansion for the top surface of the lower gold target was 0.1 mm upward and that for the bottom surface of the upper gold target was 0.1 mm downward. With a 0.1-mm margin added to these values, the gap between the upper and lower gold blocks was determined to be 0.3 mm.

The soundness of the copper blocks was evaluated in the same manner. The maximum temperature and thermal stress for the copper were 264°C and 43 MPa, respectively. The calculated thermal stress and stress amplitudes for the low and high cycles are lower than the corresponding allowable stresses. The maximum temperature rise of the stainless-steel pipes was below 100°C, and the thermal stress was sufficiently low.

Proton irradiation induces a displacement of atoms in the target material, resulting in damage that causes changes in the thermal properties and mechanical strength. Because no damage was observed in the previous target, problem-free operation of the new target is expected up to a similar irradiation level, 1.5×10^{20} protons, which corresponds to 7.4 displacements per atom at maximum in the gold, as estimated by PHITS code version 3.24 [29] with the arc-dpa model [30]. For any irradiation level, the temperature of the gold will be carefully monitored. If an obvious change is observed, the gold target can be swapped with another one, as mentioned above.

C. Monitoring equipment for new target and target chamber

The temperature of the target is monitored with thermocouples. The thermocouples were attached to the edges of each gold segment [Figs. 2(c) and 7]. The thermocouples for the most upstream gold segment are denoted channel 1 and those for the most downstream segment are denoted channel 6. Each segment contained four thermocouples. The temperatures of the cooling water pipes and the copper blocks were also monitored by thermocouples. All thermocouples were class-2 type-K sheath thermocouples, as specified in the thermocouple standard [31].

The tolerances in the standard are prescribed as ±2.5 K from −40°C up to 333°C, and $\pm 0.0075 \times T(°C)$ above 333°C. These tolerances were adopted as the errors in temperature measurements. All thermocouples were sampled every 100 ms. If the target temperature exceeds the threshold, the beam operation is stopped to avoid damage to the target. Other monitors, such as beam rate monitors and beam profile monitors, can also detect unusual beam conditions and trigger a stop in the beam operation. However, if an abnormally intense beam is injected in a few milliseconds, the maximum temperature might rise

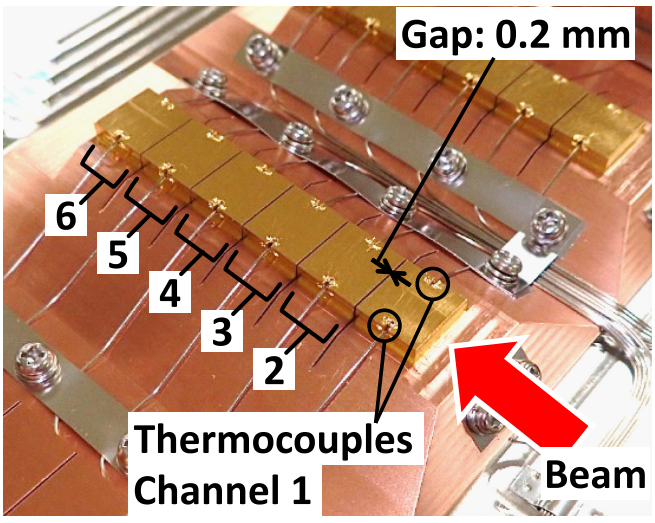

FIG. 7. Photograph of thermocouples attached to edges of each segment of gold target before final assembly. The gold target was divided into six segments along the beam direction. The thermocouples for the segments are labeled as channel 1 to channel 6, starting from the upstream.

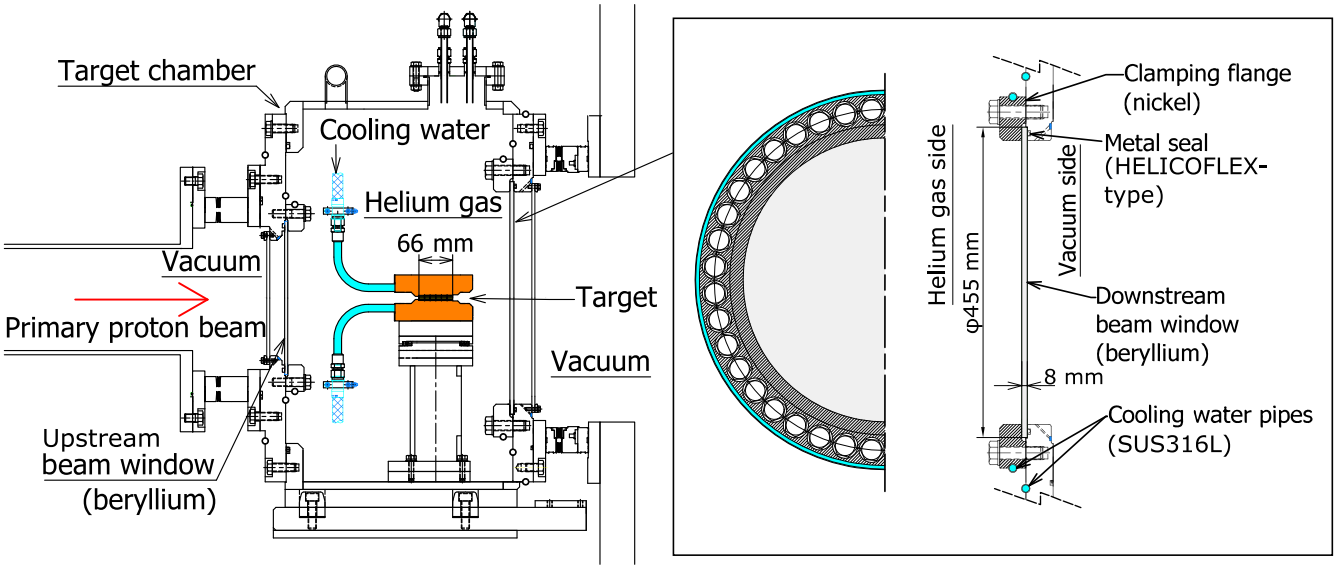

FIG. 8. Schematic drawing of target chamber in beam line with expanded view of downstream beam window.

above the melting point of the gold before the beam can be stopped. Such a beam may also cause thermal stress that is much higher than the allowable stress. The target is thus placed in a gas-tight chamber, referred to as the target chamber, to prevent the radioactive materials from spreading to the beam tunnel in the case of target failure. Figure 8 shows a schematic drawing of the target chamber in the beam line, and Figs. 9(a) and 9(b) respectively show photographs of the chamber during assembly and after the completion of major assembly. The target chamber was filled with helium gas at a pressure of around 90 kPa. The soundness of the target was monitored by measuring the amount of radioactive material contained in the gas [32].

D. Beam windows of target chamber

The beam windows, which are vacuum-tight partitions between the beam-line vacuum and the target chamber, are made of beryllium, S-200-F [33]. As shown in Fig. 8, the beam window is a simple flat disk, which is clamped onto an inner surface of the target chamber wall together with a HELICOFLEX-type metal seal [34] using a clamping flange and bolts. The upstream and downstream beryllium disks are 6 mm thick $\times 300$ mm in diameter and 8 mm thick $\times 455$ mm in diameter, respectively. The clamping flange is made of nickel (UNS-N02201) and the target chamber wall is made of stainless steel (SUS304). Cooling water pipes are attached to the target chamber wall and the downstream clamping flange (Fig. 8). In the inspection after assembly, the helium leakage rate for the beam window was smaller than the background rate, 1×10^{-10} Pa $\cdot$ m^3/s. No leakage signal was detected during beam operation.

For evaluation of the beam window soundness with a beam power of 95 kW, heat deposition in the beam window was simulated by MARS-15, and the thermal and mechanical

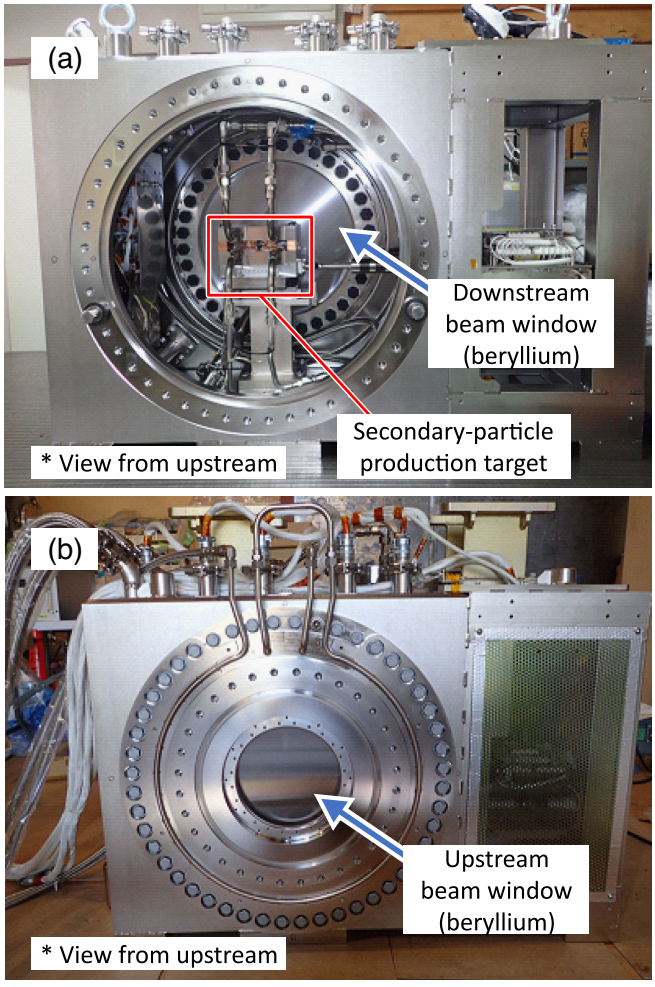

FIG. 9. (a) Photograph of target chamber with new target during assembly. (b) Photograph of target chamber from upstream side after assembly.

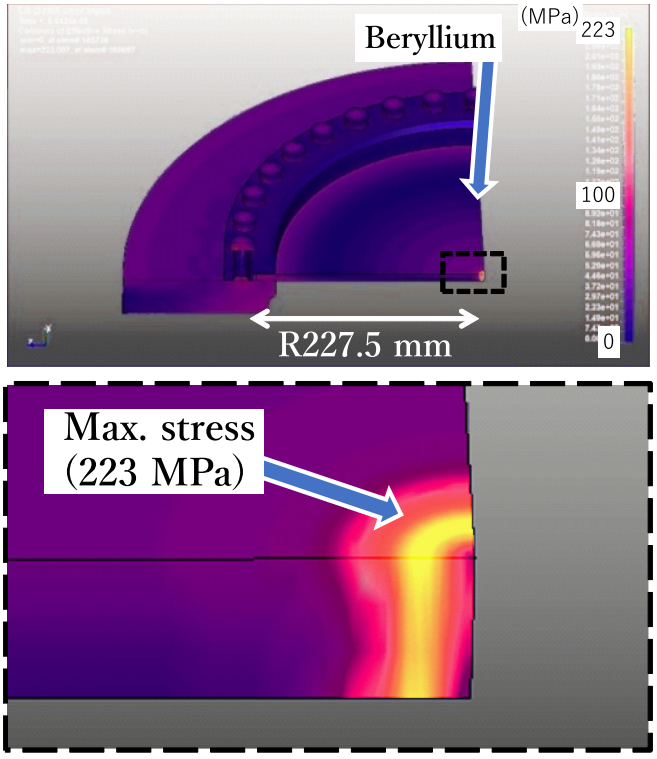

FIG. 10. von Mises stress distribution for downstream beam window for the most stringent case: abnormal beam extraction from accelerator, i.e., 5-μs-width bunched beam with power of 95 kW. The bottom figure shows an expanded cross-sectional view around the beam window center.

stresses were calculated using the finite element method with LS-DYNA R10.2 [35]. The heat deposition in the downstream beam window was estimated to be 162 W, which is much higher than that in the upstream beam window, 8.7 W, owing to the contribution of secondary particles produced in the target. In addition to the thermal load, the mechanical load generated by the pressure difference between the helium gas and vacuum and the clamping force from the metal seal and the clamping flange were applied to the beam window. For the He gas side, surface cooling by the He gas (heat transfer coefficient: 12 W/m^2/K for the upstream window and 30 W/m^2/K for the downstream window) was applied. In the evaluation, the allowable stresses were determined based on the pressure vessel standard [21]. Based on the results, the most stringent case for the beam window was found to be abnormal beam extraction from the accelerator, namely a 5-μs-width bunched beam. For the 5-μs-width bunched beam, the temperature rise of the downstream beam window was calculated to be 132°C at the beam center. Figure 10 shows the von Mises stress distribution for irradiation by a 5-μs-width bunched beam of the downstream beam window. The maximum von Mises stress in this case was estimated to be 223 MPa, which is lower than the allowable stress (282 MPa). Thus, it is concluded that the beam window will remain sound even for an abnormal bunched beam.

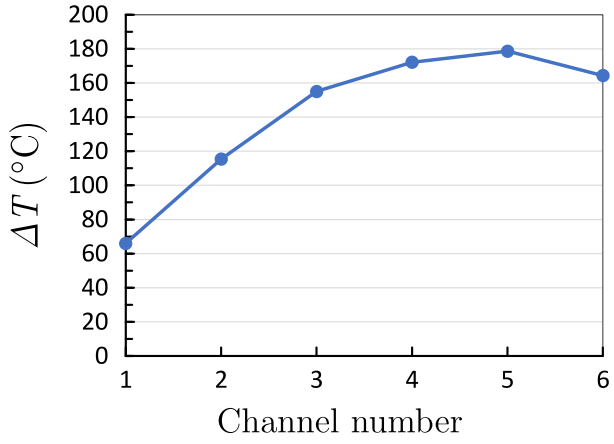

FIG. 11. Temperature rise relative to cooling water temperature vs channel number (i.e., position in beam direction) with beam power of 50 kW.

III. TEMPERATURE DATA FOR NEW TARGET DURING BEAM OPERATION

The new target was installed in the beam line in November 2019. The first beam commissioning started with a primary beam power of 5 kW in May 2020. The beam power has been increased in steps; it has thus far reached 65 kW without any problems. The distribution of the temperature rise above the cooling water temperature at 50 kW is shown in Fig. 11. Here, the vertical axis is the temperature rise averaged over the temperatures measured by the four thermocouples for each channel. As shown in the figure, the temperature rise was highest for channel 5. According to the simulation, this result is considered to be due to the loss of the primary beam and the absorption of secondary particles inside the target. Figure 12 shows the maximum temperature rises measured by the thermocouples for each beam power along with the simulation results.

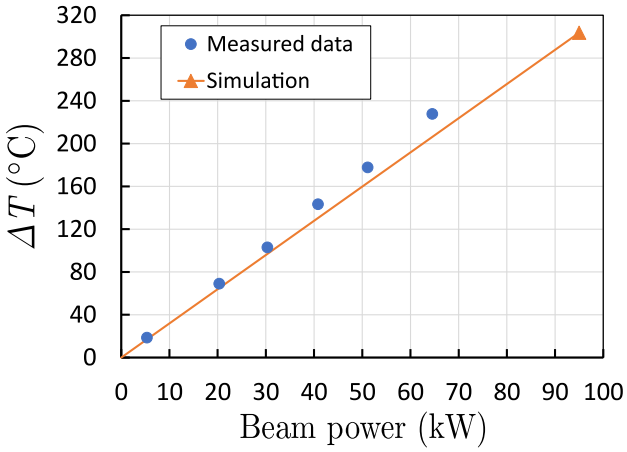

FIG. 12. Maximum temperature rise for channel 5 as a function of beam power. The result of the ANSYS simulation is also plotted for comparison.

Here, the simulation results show a temperature rise at the position of the thermocouples for channel 5 that is 12% lower than the maximum temperature rise in the gold target. The measured maximum temperatures are consistent with the simulation results to 10%.

IV. ESTIMATION OF BEAM POSITION BASED ON TARGET TEMPERATURE

As the temperature of the target was measured at four edges around the beam [Fig. 2(c)], it is possible to estimate the position of the beam based on the temperature difference between the four thermocouples. Figure 13 shows the temperature differences in the vertical and horizontal directions for channel 5 during stable beam operation with a beam power of 50 kW. The vertical difference $\Delta T_{\text{L-R}}$ and the horizontal difference $\Delta T_{\text{U-D}}$ were calculated as

$$\Delta T_{\text{L-R}} = \frac{T_{\text{UL}} + T_{\text{DL}}}{2} - \frac{T_{\text{UR}} + T_{\text{DR}}}{2} \tag{4}$$

$$\Delta T_{\text{U-D}} = \frac{T_{\text{UL}} + T_{\text{UR}}}{2} - \frac{T_{\text{DL}} + T_{\text{DR}}}{2}, \tag{5}$$

where T_{UL}, T_{UR}, T_{DL}, and T_{DR} denote the temperatures measured with the upper-left, upper-right, lower-left, and lower-right thermocouples, respectively. As shown in Fig. 13, the values of $\Delta T_{\text{L-R}}$ and $\Delta T_{\text{U-D}}$ changed during beam irradiation. The measured temperature difference is expected to show a good correlation with the beam position. The correlation was obtained by changing the beam injection position with MARS-15 used for the heat deposition simulations and ANSYS used for the temperature

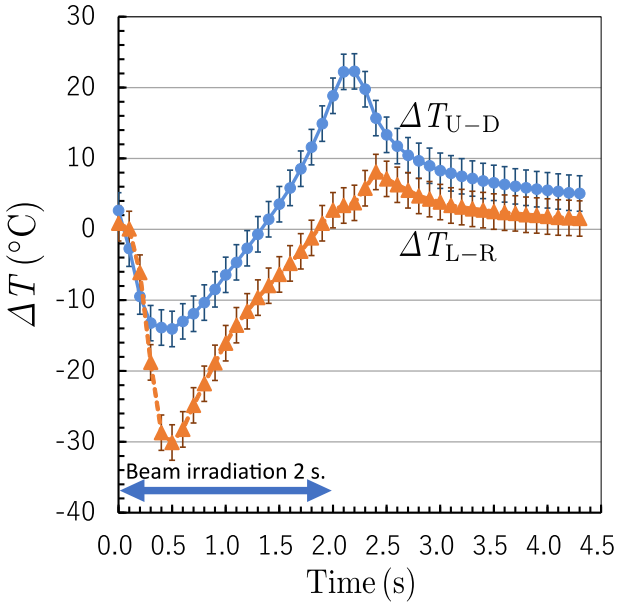

FIG. 13. Time-dependent temperature differences in horizontal and vertical directions for channel 5 with beam power of 50 kW. Time zero indicates the start of beam extraction.

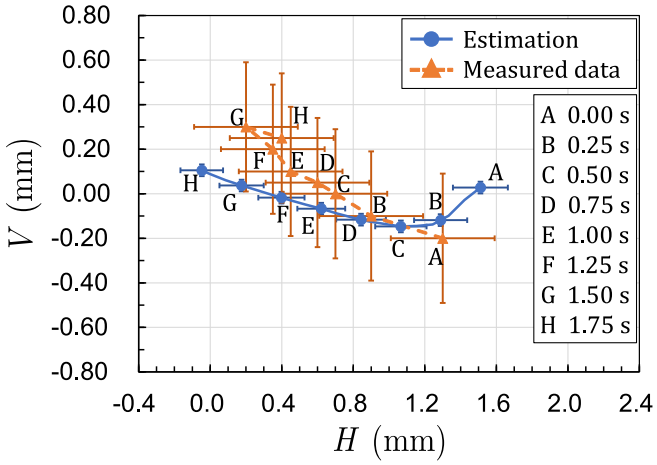

FIG. 14. Beam center positions estimated from temperature differences and measured with beam profile monitor located at about 1-m upstream of the target. Letters A through H indicate the time from the start of beam extraction.

calculations. Based on the calculation results, the beam position was estimated from the measured temperature difference. Figure 14 shows the results. For comparison, the beam positions measured by a beam profile monitor located at about 1 m upstream of the target [9] are also shown. Here, the H and V axes indicate the horizontal and vertical directions, respectively. The tendency of the position change from the lower right to the upper left between 0.5 and 1.5 s is well reproduced by the estimation. From the measurements by profile monitors located more upstream, this position change of the beam center is consistent with the change in the angle and momentum of the beam at the extraction from the MR. This result suggests that the multipoint temperature measurement of the target can be used for redundant beam position monitoring.

V. CONCLUSION

A new target for secondary-particle production was designed and manufactured to accept a more intense slowly extracted primary proton beam in the Hadron Experimental Facility at J-PARC. The target was designed so that the maximum stresses do not exceed the allowable stresses determined based on the pressure vessel standard. 95 kW is considered to be the maximum power of the primary proton beam for a 5.2-s beam duration. The new target was stably operated up to a power of 65 kW. In addition, we demonstrated that the beam position could be estimated from multipoint temperature measurements.

ACKNOWLEDGMENTS

We acknowledge continuous technical and financial support from the J-PARC Center. The design of the target system was closely reviewed by a committee at the J-PARC Center. We are grateful to the reviewers of the committee

who made valuable comments and to all who participated in the discussion. This work was supported in part by a Japan Society for the Promotion of Science Grant-in-Aid for Scientific Research (B) (Grant No. JP16H03989).

[1] Japan Proton Accelerator Research Complex, https://j-parc.jp/c/en/index.html.
[2] S. Nagamiya, Introduction to J-PARC, Prog. Theor. Exp. Phys. **2012**, 02B001 (2012).
[3] M. Ikegami, Beam commissioning and operation of the J-PARC linac, Prog. Theor. Exp. Phys. **2012**, 02B002 (2012).
[4] H. Hotchi *et al.*, Beam commissioning and operation of the Japan Proton Accelerator Research Complex 3-GeV rapid cycling synchrotron, Prog. Theor. Exp. Phys. **2012**, 02B003 (2012).
[5] K.-D. Liss, *Materials and Life Science Experimental Facility (MLF) at the Japan Proton Accelerator Research Complex (J-PARC)* (Quantum Beam Science, Basel, 2019), 10.3390/books978-3-03897-484-0.
[6] T. Koseki *et al.*, Beam commissioning and operation of the J-PARC main ring synchrotron, Prog. Theor. Exp. Phys. **2012**, 02B004 (2012).
[7] T. Sekiguchi, Neutrino facility and neutrino physics in J-PARC, Prog. Theor. Exp. Phys. **2012**, 02B005 (2012).
[8] Hadron Experimental Facility, https://j-parc.jp/c/en/facilities/nuclear-and-particle-physics/hadron.html.
[9] K. Agari *et al.*, Primary proton beam line at the J-PARC Hadron Experimental Facility, Prog. Theor. Exp. Phys. **2012**, 02B008 (2012).
[10] H. Ohnishi, F. Sakuma, and T. Takahashi, Hadron physics at J-PARC, Prog. Part. Nucl. Phys. **113**, 103773 (2020).
[11] T. Yamanaka (KOTO Collaboration), The J-PARC KOTO experiment, Prog. Theor. Exp. Phys. **2012**, 02B006 (2012).
[12] K. Agari *et al.*, Secondary charged beam lines at the J-PARC hadron experimental hall, Prog. Theor. Exp. Phys. **2012**, 02B009 (2012).
[13] T. Takahashi *et al.*, Beam and SKS spectrometers at the K1.8 beam line, Prog. Theor. Exp. Phys. **2012**, 02B010 (2012).
[14] K. Agari *et al.*, The K1.8BR spectrometer system at J-PARC, Prog. Theor. Exp. Phys. **2012**, 02B011 (2012).
[15] T. Shimogawa (KOTO Collaboration), Design of the neutral K^0_L beamline for the KOTO experiment, Nucl. Instrum. Methods Phys. Res., Sect. A **623**, 585 (2010).
[16] H. Takahashi *et al.*, Indirectly water-cooled production target at J-PARC hadron facility, J. Radioanal. Nucl. Chem. **305**, 803 (2015).
[17] H. A. Saller, S. J. Paprocki, R. W. Dayton, and E. S. Hodge, Method of Bonding, U.S. Patent No. 4,709,848.
[18] H. V. Atkinson and S. Davies, Fundamental aspects of hot isostatic pressing: An overview, Metall. Mater. Trans. A **31**, 2981 (2000).
[19] J. Busom Descarrega, M. Calviani, T. Hutsch, E. López Sola, A. T. Pérez Fontenla, A. Perillo Marcone, S. Sgobba, and T. Weißgärber, Application of hot isostatic pressing (HIP) technology to diffusion bond refractory metals for proton beam targets and absorbers at CERN, Mater. Des. Process. Commun. **2**, e101 (2020).
[20] S. Pianese *et al.*, Hot isostatic pressing assisted diffusion bonding for application to the Super Proton Synchrotron internal beam dump at CERN, Phys. Rev. Accel. Beams **24**, 043001 (2021).
[21] Japanese Industrial Standard, Alternative standard for construction of pressure vessels, JIS B 8266, Japanese Standards Association, Tokyo, 2003.
[22] N. E. Frost, K. J. Marsh, and L. P. Pook, *Metal Fatigue* (Clarendon Press, Oxford, 1974).
[23] R. D. McCammon and H. M. Rosenberg, The fatigue and ultimate tensile strengths of metals between $4 \cdot 2$ and 293°K, Proc. R. Soc. A **242**, 203 (1957).
[24] Japanese Industrial Standard, Metallic materials -Tensile testing- Method of test at room temperature, JIS Z 2241, Japanese Standards Association, Tokyo, 2011.
[25] N. V. Mokhov and C. C. James, The Mars code system user's guide version 15(2016), Report No. Fermilab-FN-1058-APC, 2017.
[26] N. V. Mokhov, P. Aarnio, Y. Eidelman, K. Gudima, A. Konobeev, V. Pronskikh, I. Rakhno, S. Striganov, and I. Tropin, MARS15 code developments driven by the intensity frontier needs, Prog. Nucl. Sci. Technol. **4**, 496 (2014).
[27] ANSYS, http://www.ansys.com/.
[28] J. Bree, Elastic-plastic behaviour of thin tubes subjected to internal pressure and intermittent high-heat fluxes with application to fast nuclear-reactor fuel elements, J. Strain Anal. Eng. Des. **2**, 226 (1967).
[29] Tatsuhiro Sato *et al.*, Features of particle and heavy ion transport code system (PHITS) version 3.02, J. Nucl. Sci. Technol. **55**, 684 (2018).
[30] Y. Iwamoto, S. Meigo, and S. Hashimoto, Estimation of reliable displacements-per-atom based on athermal-recombination-corrected model in radiation environments at nuclear fission, fusion, and accelerator facilities, J. Nucl. Mater. **538**, 152261 (2020).
[31] Japanese Industrial Standard, Thermocouples, JIS C 1602, Japanese Standards Association, Tokyo, 2015.
[32] R. Muto *et al.*, Monitoring system for the gold target by radiation detectors in Hadron Experimental Facility at J-PARC, EPJ Web Conf. **153**, 07004 (2017).
[33] Beryllium S-200-F, Materion Corp., https://materion.com/.
[34] HELICOFLEX-type seal, Technetics Group, https://technetics.com/products/helicoflex-metal-resilient-seal/.
[35] LS-DYNA, https://lstc.com/products/ls-dyna.